RESEARCH ARTICLE | OCTOBER 07 2025

Surface-normal photonic crystal waveguide arrays for ultra-sensitive mid-IR gas sensing

Kang-Chieh Fan ; Jason Midkiff; May Hlaing ; Sourabh Jain ; Ray T. Chen

AIP Advances 15, 105009 (2025)
https://doi.org/10.1063/5.0277786

Surface-normal photonic crystal waveguide arrays for ultra-sensitive mid-IR gas sensing

Cite as: AIP Advances 15, 105009 (2025); doi: 10.1063/5.0277786
Submitted: 16 May 2025 • Accepted: 10 September 2025 •
Published Online: 7 October 2025

Kang-Chieh Fan,[1] Jason Midkiff, May Hlaing, Sourabh Jain,[3] and Ray T. Chen[1,2,a)]

AFFILIATIONS

[1] Department of Electrical and Computer Engineering, University of Texas at Austin, Austin, Texas 78758, USA
[2] Omega Optics, Inc., 8500 Shoal Creek Blvd., Bldg. 4, Suite 200, Austin, Texas 78757, USA
[3] Department of Electronics and Communication Engineering, Indian Institute of Information Technology, Bhopal, Madhya Pradesh, India

[a)] **Author to whom correspondence should be addressed:** chenrt@austin.utexas.edu

ABSTRACT

This paper presents a novel silicon-based hollow-core surface-normal photonic crystal waveguide with an air-core even mode and high group index in the meta structure. This mode is proposed for gas detection in the mid-infrared range. The structure's bandgap map and guided modes were calculated through numerical simulations, allowing for design optimization to enable slow-light propagation of the guided modes. The design enhances light–matter interaction by leveraging large group indices and dispersion control. In experimental simulations of photonic crystal waveguide structures, an ultra-high group index of 1424 was achieved at a wavelength of 3.31 μm, matching with methane absorption. This high group index—i.e., the realization of extremely slow light—facilitates enhanced interaction with analytes of interest. The result reveals that 60.1% of the energy of the fundamental mode resides within the center air hole, providing a high overlap with analytes. The device geometry can be customized to introduce the absorption wavelengths of various analytes, enabling arrays of different device geometries on the same chip for simultaneous detection of multiple gas species.

I. INTRODUCTION

Since the advent of photonic crystal fibers (PCFs) in the 1990s,[1,2] they have attracted attention for their unique optical properties unattainable with traditional optical fibers. Conventional optical fibers guide light through total internal reflection (TIR) in a core with a higher refractive index than the surrounding cladding. However, directing light through a hollow core can significantly reduce losses from scattering and material absorption.[3] To confine and guide light in this low-index region, hollow-core photonic bandgap fibers (HC-PBGFs) were developed. HC-PBGFs utilize the photonic bandgap effect—instead of index-guiding—to confine light within the hollow core via Bragg reflection from periodic cladding layers. This architecture enables single-mode guidance, customizable dispersion, larger mode areas, and increased confinement factors.

The photonic bandgap offers numerous fascinating properties, such as light confinement at low index point and line defects, constraints on operating frequencies, and the slow-light phenomenon. By modifying the medium, one can manipulate the dispersion characteristics, decelerate the light, or even effectively halt it.[4] Known for providing slow light propagation in line-defect waveguides, photonic crystals are poised for a wide array of applications.[5] These include optical storage, switching, and sensing, where the slow-light effect can be particularly advantageous.[6–9]

Despite significant progress in photonic crystal-based sensing, current approaches face fundamental limitations that restrict their practical implementation. Existing HC-PBGFs, while demonstrating gas sensing capabilities through enhanced light–matter interactions in air-filled cores,[10] are constrained by the inherently narrow photonic bandgaps achievable with silica-based materials due to low-index contrast. On the another hand, leveraging the high core-cladding index contrast in Si based photonic crystal platform, significant improvement in sensitivity through slow-light enhancement has been reported,[11] yet these implementations primarily utilize

in-plane waveguide geometries that present critical challenges: (1) complex optical coupling requirements that limit system integration, (2) restricted access to the sensing volume for gas injection and collection, (3) moderate group index enhancements that are insufficient for ultra-high sensitivity applications, and (4) incomplete bandgap coverage that limits operational bandwidth and slow-light performance. Furthermore, no previous work has demonstrated surface-normal photonic crystal configurations that can simultaneously achieve ultra-high group indices exceeding 1000 while maintaining direct surface access for gas interaction—representing a significant gap in the field.

In the past, the predominant material of choice for the fabrication of photonic crystal fibers has been silica-based glass, owing to the well-established nature of silica glass-based optical fiber manufacturing processes. With a refractive index (n_{silica}) of ~1.44, silica inherently yields only narrow photonic bandgaps. However, recent years have witnessed remarkable advancements in semiconductor manufacturing technologies, catalyzing the progression of silicon photonics. Consequently, the utilization of silicon as a waveguide material has emerged. Silicon boasts a considerably higher refractive index (n_{silicon}), thus enabling larger refractive index contrast (Δn) values when employed as the foundational material for photonic crystals. This attribute empowers silicon photonic crystals to exhibit broader photonic bandgaps, representing a pivotal advancement in the field. Addressing these critical limitations, there is an urgent need for a photonic crystal gas sensing platform that combines the advantages of silicon's high refractive index contrast with a surface-normal configuration for practical implementation. Such a platform must achieve unprecedented slow-light enhancement while providing direct access to the sensing volume—capabilities that remain absent in current state-of-the-art systems.

This work introduces a surface-normal photonic crystal waveguide (SUNPCW) made of silicon, designed with a structure akin to HC-PBGFs, specifically for gas detection leveraging the porosity of the structure. This SUNPCW features a cladding composed of perfectly periodic air holes yielding a two-dimensional photonic crystal, creating bandgaps at designed frequencies. Unlike HC-PBGFs, which are typically constructed from low-index contrast materials such as silica glass and air and do not support a complete bandgap for both polarizations at small propagation constants (k),[12] silicon displays unique dispersion characteristics. It allows creation of a complete bandgap extending to $k = 0$, where ultra-low group velocity ($v_g = d\omega/dk$) is observed. By customizing the defect core surrounded with microstructured cladding, we can guide light at specific wavelengths through the air core with a reduced group velocity. The hollow core of this waveguide is capable of accommodating both the optical mode and gas species, significantly enhancing interactions between photons and analytes. With its high group indices ($n_g = c/v_g$) and large mode area, this device is exceptionally well-suited for gas sensing applications in the mid-infrared range with unprecedented sensitivity.

The field of mid-infrared (mid-IR) photonics has a wide range of applications, including thermal imaging, free-space communications, medical diagnostics, bio-agent detection, and absorption spectroscopy. Unlike the near-infrared spectrum, where absorption peaks are typically overtones, the mid-infrared range allows for probing gas species at their fundamental resonances. Traditional commercial absorption spectroscopy systems, such as non-dispersive infrared (NDIR) gas sensing,[13] Fourier transform infrared (FTIR) spectroscopy,[14] tunable direct laser absorption spectroscopy (TDLAS),[15] cavity ring-down spectroscopy (CRDS),[16] and photo-acoustic spectroscopy (PAS),[17] tend to involve bulky and costly optical components. An on-chip absorption spectroscopy approach offers a compact, alignment-free alternative, resulting in a lightweight spectrometer ideal for applications requiring low size, weight, power, and cost (SWaP-C).

II. DEVICE DESIGN AND WORKING PRINCIPLE

To study the peculiar photonic band structure (the dispersion relation between frequency and wavevector) and the corresponding guided modes of the SUNPCW, we carried out plane wave expansion (PWE) simulations using MIT Photonic Bands (MPBs) and finite difference eigenmode (FDE) simulations using Ansys Lumerical MODE.

A. Photonic bandgap

MIT photonic bands calculate the dispersion relation and various electromagnetic modes in periodic dielectric structures, including modes arising from defects. MPBs have been applied for calculating two two-dimensional structures: (a) a photonic crystal made up of a hexagonal lattice of silicon rods and (b) a photonic crystal made up of a hexagonal lattice of air holes in silicon. For both structures, the period is set as a and the radius r of silicon rod or air hole is set to $0.47a$, as shown in Fig. 1.

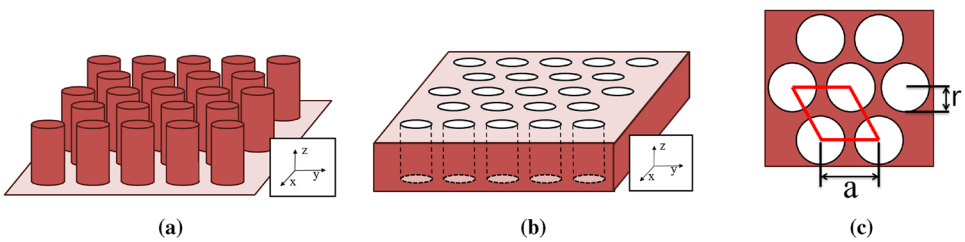

FIG. 1. A two-dimensional photonic crystal structure and the dimension. (a) The structure consists of hexagonal silicon rods, with radius r. The silicon rods are homogeneous along the z direction. (b) A photonic crystal consisting of air columns is embedded in a silicon substrate, assumed to extend infinitely in the out-of-plane z direction. Each column has a radius r and a dielectric constant $\varepsilon = 1$. (c) A top-down view of the hexagonal lattice, highlighting the unit cell outlined in red. The lattice constant is denoted as a.

Figure 2(a) plots the MPB simulation results for the silicon rod structure, with frequency plotted in dimensionless units as $\omega a/2\pi c$, where ω is the angular frequency, a is the lattice constant, and c is the speed of light. As revealed, there are transverse magnetic (TM) mode and transverse electric (TE) mode bandgaps without any overlap. Figure 2(b) shows the band structure diagram for the photonic crystal with a hexagonal lattice comprising air holes in a silicon slab. Cross-hatched regions correspond to bandgaps, and the band structure diagram exhibits significant bandgaps for both polarizations. As a result, contrary to the silicon rod structure, this photonic crystal supports a complete and overlapping bandgap for both polarizations in two dimensions. The TM and TE bandgaps occur at frequencies of 0.27–0.46 and 0.38–0.40 ($\omega a/2\pi c$), respectively, with the overlapping frequency range extending from 0.38 to 0.40 ($\omega a/2\pi c$).

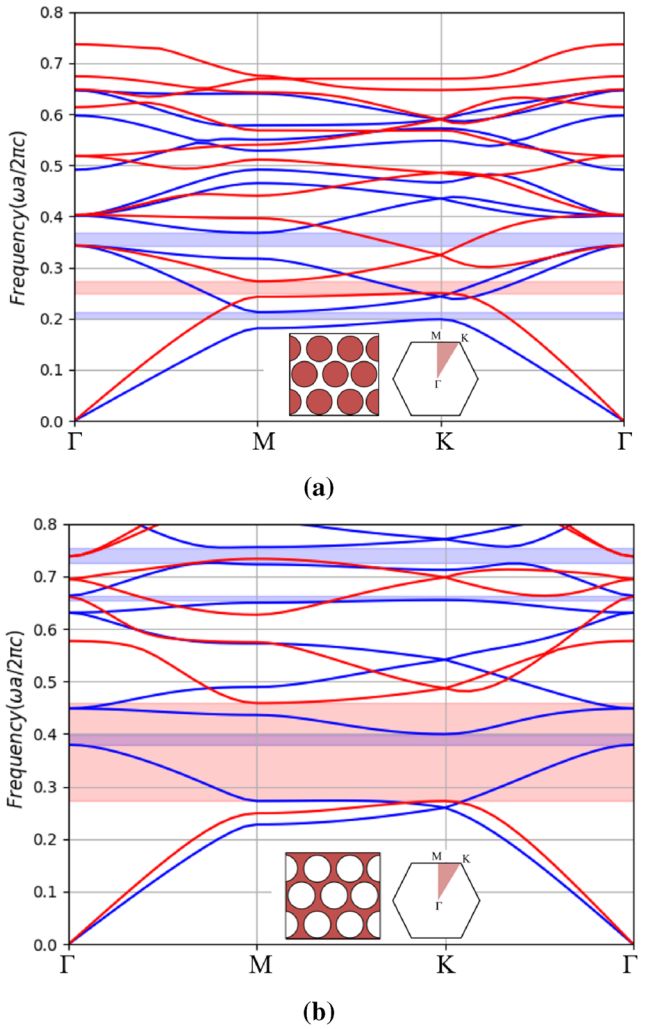

FIG. 2. (a) Band structure diagram of the photonic crystal with hexagonal lattice silicon rod structure. (b) Band structure diagram of the photonic crystal with hexagonal lattice air hole structure. Red solid lines represent TE bands, and blue solid lines represent TM bands. The red area shows the TE bandgap, while the blue area represents the TM bandgap. The radius of the rods or holes is set to r = 0.74a, where a is the lattice constant. Unlike the silicon rod structure, the air hole photonic crystal features a complete overlapping bandgap for both polarizations.

Figure 3 illustrates that larger bandgaps are associated with larger refractive indices. This correlation supports the growing trend of utilizing materials such as silicon for photonic crystal production. With a refractive index of ~3.43, silicon differs markedly from lower-index materials such as silica, where it has the potential to develop wider bandgaps.

The photonic bandgap plays a crucial role in the physics of photonic crystals. When light encounters a photonic bandgap, it adheres to the principle of energy conservation and reflects entirely instead of being absorbed or transmitted. This complete reflection ensures that there is no loss of energy. In essence, the photonic bandgap acts as a barrier to certain frequencies of light, preventing them from propagating through the crystal. In practical applications, the selection of specific bandgaps is of paramount importance. In this case, the focus is on the overlapping photonic bandgaps of TM/TE modes. These modes represent the two fundamental polarization states of light in the crystal. By targeting these overlapping bandgaps, it becomes possible to manipulate and control the propagation of light within the photonic crystal. Upon introducing a defect into the crystal, the behavior of light propagation undergoes a significant change. The defect alters the symmetry of the crystal structure, creating a localized region where the propagation characteristics differ from the rest of the crystal. What is particularly noteworthy is that because of the existence of the photonic bandgaps for both TM/TE modes, light is effectively confined within the defect structure. Regardless of whether the light is in the TM or TE orientation, the presence of these photonic bandgaps serves as a boundary that confines the light within the defect. This confinement enables the light to propagate within the defect structure, providing a controlled pathway for the light and allowing for the manipulation of its properties for various applications.

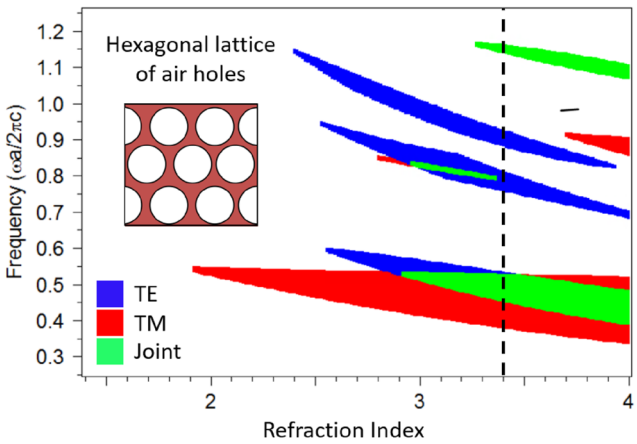

FIG. 3. The bandgap map for a hexagonal lattice of air holes. The joint region, highlighted in green, appears only when the refractive index exceeds 3. The dashed line indicates the case for a refractive index of 3.43, which corresponds to that of silicon. High-refractive-index materials play a crucial role in enabling the creation of significantly wider TM/TE joint bandgaps.

B. Surface-normal photonic crystal waveguide

While controlling in-plane propagation is advantageous for many applications, we propose leveraging and controlling out-of-plane (i.e., vertical) propagation for gas sensing. This approach offers distinct benefits, including enhanced interaction with target gas molecules, improved sensor sensitivity, and greater flexibility in device integration. The following sections will elaborate on these advantages in detail.

In order to study the effect of the out-of-plane propagation constant on the complete bandgap width, the band structure computation is performed as the normalized k_z is swept from 0 to 2, where k_z is the wave vector along the z-direction and the normalization is given by $k_z a/(2\pi)$, with a being the lattice constant. Figure 4 illustrates the resulting bandgaps occurring between different bands (color-coded). As revealed by the bandgap diagram, there exists a complete bandgap in this structure that does not pinch off before reaching $k_z = 0$ as the propagation constant decreases. The blue region represents the bandgap between the second and third bands, extending to $k_z = 0$, while the orange region corresponds to the bandgap between the seventh and eighth bands.

Now that the bandgaps have been established, the next step involves introducing a defect into the crystal structure. By introducing an enlarged-hole defect, we can achieve both slow light propagation and the formation of a sizable interaction volume for gas sensing. A top-view schematic representation of the hexagonal photonic crystal with the hollow-core defect is depicted in Fig. 5.

To investigate the vertically guided defect modes inside the bandgap, eigenvalues for guided modes were calculated. Using the MPB software, we computed the band diagram, which plots the normalized frequency as a function of the out-of-plane wavevector for the hexagonal lattice photonic crystal with a defect. The photonic crystal structure, as shown in Fig. 5, has a defect radius (D) of $1.22a$, where a is the lattice period constant, and an air-hole radius (r) of $0.47a$.

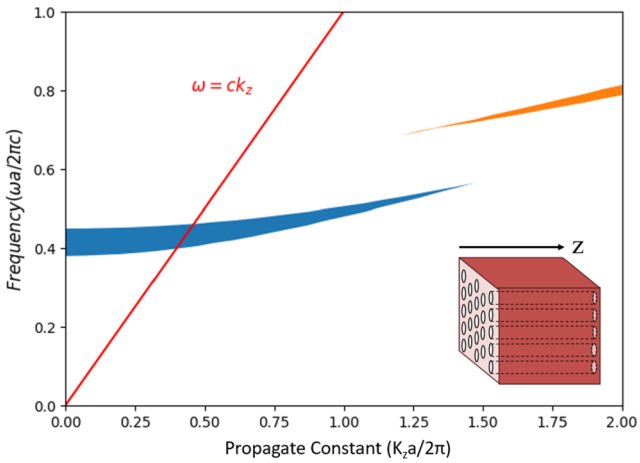

FIG. 4. Bandgaps as a function of normalized propagation constant. Bandgaps occurring between different color-coded bands. The blue-hatched region represents the bandgaps that extend to $k_z = 0$.

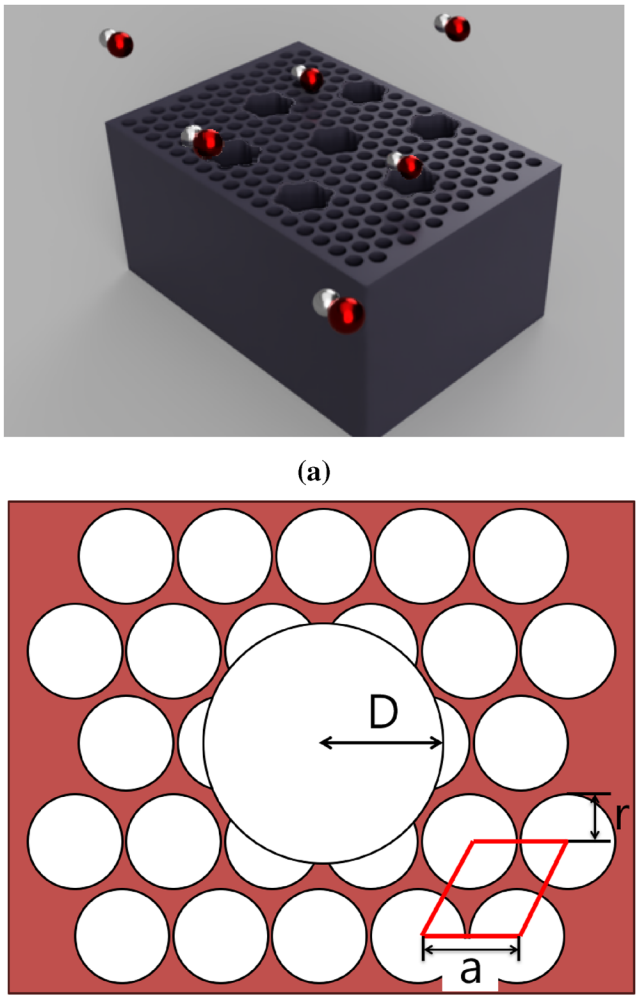

FIG. 5. (a) Schematic illustration of the SUNPCW with hollow-core defect. (b) Dimension of photonic crystal structure.

Figure 6 demonstrates the bands computed for wavevectors ranging from 0 to 0.6 $(k_z a/2\pi)$, revealing several band lines located within the bandgap, with frequencies ranging from 0.38 to 0.45 $(\omega a/2\pi c)$. To determine the most appropriate guided mode for gas sensing applications, the interaction between light and gas molecules must be considered. Effective gas sensing requires that the power of the light be concentrated in the central air core rather than propagating within or along the surface of the solid material.

According to Fig. 7, most of the guided modes operate in the latter manner. An "air-core mode" refers to a guided mode where light is predominantly confined and propagates through the air-filled region of the structure. Although these modes conform to mathematical calculations, in practical applications, they face coupling challenges and have high transmission loss. However, a few of the modes demonstrate power propagation primarily through the defect hole (i.e., the hollow core). As depicted in Figs. 7(a)–7(d),

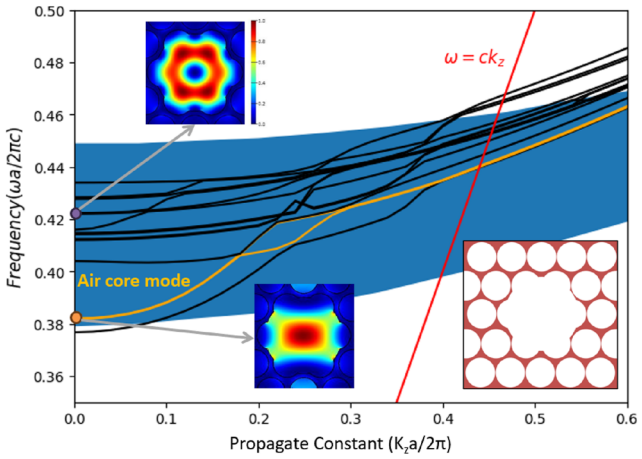

FIG. 6. Band diagram of the surface-normal photonic-crystal waveguide. Black solid lines are the computed guided-mode bands; the blue shaded region marks the projected bandgap of the 2D photonic crystal. The orange curve highlights the hollow-core even mode ("air-core mode") under study. The red diagonal line is the light line, $\omega = ck_z$. Insets show the corresponding electric field intensity profiles at those two dots, which indicate the modes plotted in Fig. 7.

these instances show a distinct propagation pattern where the electromagnetic energy is concentrated in the defect hole of the waveguide structure. It is important to note that while the resonant modes are presented for $k_z = 0$, the out-of-plane propagating modes for small k_z are small perturbations of these modes.

C. Guided mode profiles

Subsequently, we observed several intensity patterns of modes, prompting further investigation into the mode profiles. To achieve this, we utilized the software Lumerical MODE from Ansys, which facilitated the identification and evaluation of the modes' efficacy. This step is crucial for determining which modes are optimally suited for gas sensing and understanding their propagation characteristics within the SUNPCW structure.

The FDE solver of Lumerical MODE is a numerical technique used to find the eigenmodes and corresponding eigenfrequencies of waveguide structures, optical devices, and other systems in the context of electromagnetics or photonics. The eigensolver identifies these modes through the resolution of Maxwell's equations on a mesh representing the waveguide's cross section.

Currently, the finite-difference algorithm serves as the primary approach for discretizing the waveguide's geometry, and it possesses the capability to adapt to various waveguide structures. After the meshing process is complete, Maxwell's equations are reformulated into a matrix eigenvalue problem. Sparse matrix techniques are then applied to solve this problem, yielding the effective index and mode profiles for the waveguide modes.[18]

The guided mode simulations presented in this study were conducted using *Ansys Lumerical MODE Solutions*, employing the Finite Difference Eigenmode (FDE) solver. The computational domain utilized a uniform mesh resolution of 10 nm in both the x and y directions, carefully selected based on convergence studies to ensure accurate and stable simulation results. The simulation region spanned five photonic crystal periods in each lateral direction, with periodic boundary conditions applied to model the infinite

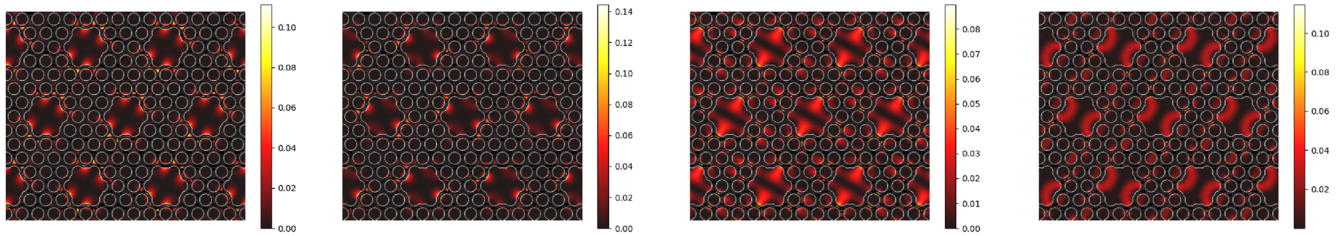

FIG. 7. Intensity pattern $(\hat{z} \cdot \mathrm{Re}[E^* \times H])$ $(k_z = 0)$ (a) $\omega a/2\pi c = 0.3818$ and (b) $\omega a/2\pi c = 0.3820$, corresponding to the yellow dot in Fig. 6, and (c) $\omega a/2\pi c = 0.4277$, (d) $\omega a/2\pi c = 0.4287$, and (d) $\omega a/2\pi c = 0.4221$, corresponding to the purple dot in Fig. 6. The intensity patterns (a)–(d) are above the light line and are the air core.

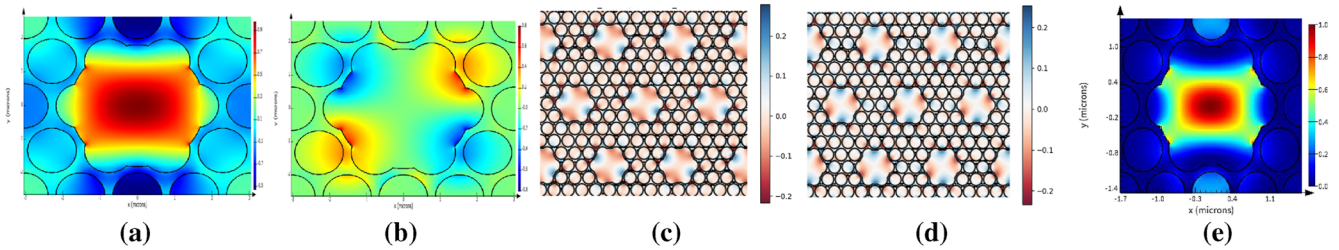

FIG. 8. Even air-core mode profile, corresponding to yellow dot in Fig. 6. (a) and (b) The electric field components in the x and y directions, respectively, calculated using FDE method. (c) and (d) The electric field components in the x and y directions, respectively, as computed by MPB method. (e) The electric intensity mode.

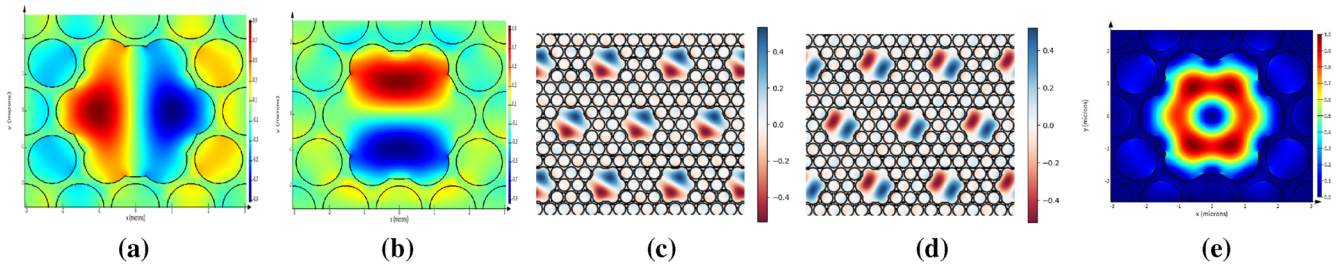

FIG. 9. Odd air-core mode profile, corresponding to purple dot in Fig. 6. (a) and (b) The electric field components in the *x* and *y* directions, respectively, calculated using FDE method. (c) and (d) The electric field components in the *x* and *y* directions, respectively, as computed by MPB method. (e) The electric intensity mode.

periodic nature of the structure and suppress artificial reflections at the domain edges.

To ascertain the mode profiles of the SUNPCW, specific structural parameters were defined for the photonic crystal structure, as shown in Fig. 5. The operating wavelength was set at 3.31 μm, targeting methane sensing applications. The periodicity of the photonic crystal (a) was established at 0.8563 μm. The radius of the air holes (r) was set to 0.3682 μm, and the radius of the central defect hole (D) was configured at 1.0446 μm. These geometric parameters are critical as they determine the optical confinement and propagation characteristics of the guided modes within the photonic crystal waveguide structure. Material properties used in the simulations were based on standard literature values: the refractive index of silicon was taken from the material library,[19] yielding $n = 3.43$ at a target wavelength of 3.31 μm, and the refractive index of air was set to $n = 1.0$.

The air-core mode profiles obtained from the FDE simulations are compared with the corresponding results derived using the MPB method. Figure 8 shows the even air-core mode profile (corresponding to the yellow dot in Fig. 6), where Figs. 8(a) and 8(b) illustrate the electric field components in the *x* and *y* directions as calculated by the FDE method, while Figs. 8(c) and 8(d) showcase these components as computed by the MPB method. Figure 8(e) presents the electric intensity mode for this even mode. Similarly, Fig. 9 displays the odd air-core mode profile (corresponding to the purple dot in Fig. 6), with Figs. 9(a) and 9(b) showing the electric field components in the *x* and *y* directions calculated by the FDE method and Figs. 9(c) and 9(d) presenting the MPB method results. The electric intensity mode for the odd mode is illustrated in Fig. 9(e). A critical observation from these comparisons is the remarkable consistency between the two sets of results, particularly in the representation of both even and odd air-core modes' electric fields.

The transportation of electromagnetic power is fundamentally governed by a vector known as the Poynting vector. This vector not only represents the direction but also quantifies the magnitude of the energy flux of an electromagnetic field. Figure 10 illustrates the Poynting vector results calculated by the FDE method. These results are focused on the *z*-direction, which represents the primary direction of wave propagation along the hollow core waveguide. A notable observation from Fig. 10 is the pronounced concentration of electromagnetic energy within the waveguide defect, specifically located at the center of what is termed the "air core."

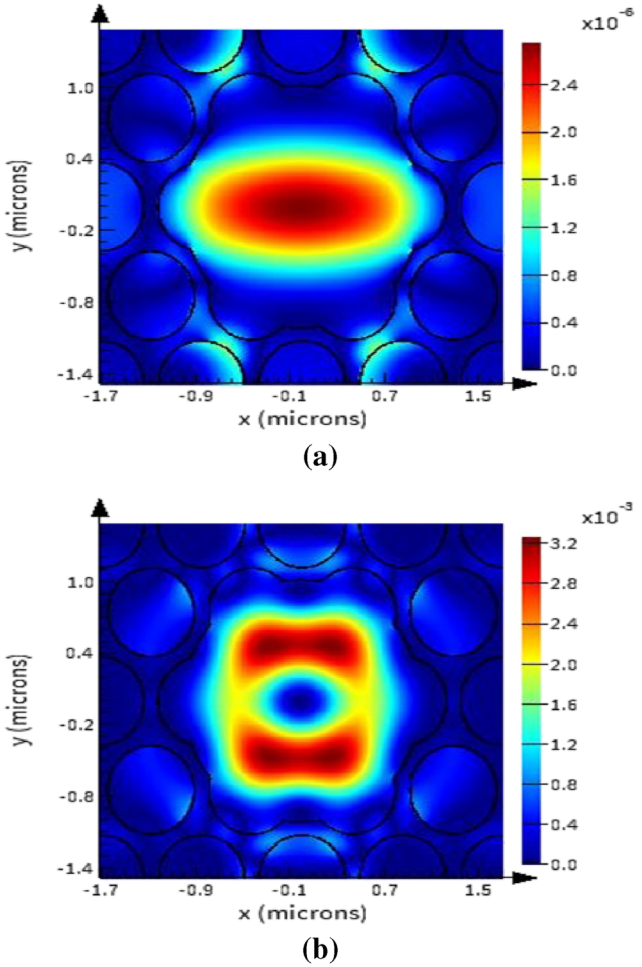

FIG. 10. Poynting vector calculated by finite difference eigenmode method. (a) Even air-core mode. (b) Odd air-core mode.

This study identifies an air-core mode, as shown in Fig. 10(a) that exhibits "even mode" characteristics. In our setup, the incident light generally used is a laser with a Gaussian mode profile carrying the characteristic of an even function. In terms of optical coupling,

TABLE I. Group indices for specific gases at absorption wavelengths in a SUNPCW structure.

Gas[a]	a (μm)[b]	r (μm)[c]	D (μm)[d]	n_g
CH_4	0.8563	0.3682	1.0446	1424
CO_2	1.0997	0.4728	1.3416	866
N_2O	1.1566	0.4973	1.4111	698

[a]Absorption wavelengths: CH_4 at 3.31 μm, CO_2 at 4.26 μm, and N_2O at 4.54 μm.
[b]a is the lattice period.
[c]r is the air-hole radius.
[d]D is the defect hole radius.

the efficiency of coupling into an even mode is high. Therefore, identifying an even mode can enhance the efficiency of transferring the incident light into the sensing area. The goal is to transmit more energy through the air for interaction with airborne species, making an even air-core mode crucial. The MPB PWE and Lumerical MODE FDE results confirm these modes.

Our focus extends to the detection of specific gases—methane (CH_4), carbon dioxide (CO_2), and nitrous oxide (N_2O)—which absorb light at wavelengths of 3.31, 4.28, and 4.47 μm, respectively. The simulation parameters and outcomes, presented in Table I, demonstrate that the group indices for these gases can reach values of 1423, 866, and 698, respectively. These high values are indicative of the air-core mode's ability to produce a significant slow-light effect within the vertical photonic crystal waveguide structure. This slow-light effect is crucial for enhancing sensitivity. By achieving such high group indices, the SUNPCW is able to maintain light within its structure for extended periods, which is particularly advantageous for the detection and analysis of these gases based on their specific absorption wavelengths. The ability to tailor the waveguide to effectively interact with these gases underscores the versatility and potential applicability of this technology in environmental monitoring and gas sensing.

III. GAS SENSING PRINCIPLE AND DEMONSTRATION

The surface-normal photonic crystal waveguide (SUNPCW) structure enables effective gas sensing by leveraging the wavelength-selective absorption characteristics intrinsic to target gas molecules. When mid-infrared (mid-IR) light propagates through the engineered hollow-core defect of the waveguide, it interacts with gas analytes such as CH_4 and CO_2. These molecules exhibit distinctive absorption peaks at specific mid-IR wavelengths that correspond to their fundamental molecular vibrational modes. This engineered hollow-core defect of the waveguide supports slow light modes, which significantly reduces the group velocity of the propagating light. This slow-light effect increases the effective interaction time between the optical field and the gas analytes. Therefore, the absorption signal is enhanced without increasing the physical footprint of the sensor.

The fundamental sensing mechanism is quantitatively described by the Beer–Lambert law. This law relates the optical intensity transmitted through the sensing medium to the concentration of the absorbing species according to

$$I = I_0 e^{-\alpha(\lambda) L_{eff}}, \tag{1}$$

where I represents the transmitted intensity, I_0 denotes the initial optical intensity entering the sensing region, $\alpha(\lambda)$ is the wavelength-dependent absorption coefficient specific to the gas analyte, and L_{eff} signifies the effective optical length. The effective optical length is given by

$$L_{eff} = n_g \cdot L, \tag{2}$$

where n_g is the group index and L is the optical length (i.e., the physical distance over which light interacts with the gas).

The effective optical length is significantly influenced by the group index, allowing the slow-light effect to substantially increase the effective optical length and thereby enhance sensing sensitivity. For example, when sensing CH_4 with a group index of $n_g = 1424$ and a physical optical length of $L = 1$ μm, the effective optical length becomes $L_{eff} = 1424 \times 1$ μm $= 1.424$ mm. This represents a remarkable sensitivity enhancement factor of 1424 compared to conventional sensing approaches, where the enhancement factor directly corresponds to the group index value. The slow-light enhancement mechanism enables dramatically improved sensitivity within an extremely compact sensing volume, making the SUNPCW structure highly advantageous for miniaturized gas sensing applications.

Building upon this enhanced sensitivity principle, the SUNPCW array (depicted in Fig. 11) can be systematically designed with varying structural scales to form multiple resonance channels, each optimized for detecting different gases. In this configuration, the photonic crystal array incorporates multiple waveguides with proportionally scaled crystal lattices and defect holes that serve as sensing sites, exposed directly to the target gas molecules. The scaling of the entire photonic crystal structure—including both the periodic lattice and the central defect—enables wavelength tunability while maintaining optimal optical confinement. These defect holes enable gas infiltration, facilitating strong interaction with the guided electromagnetic field.

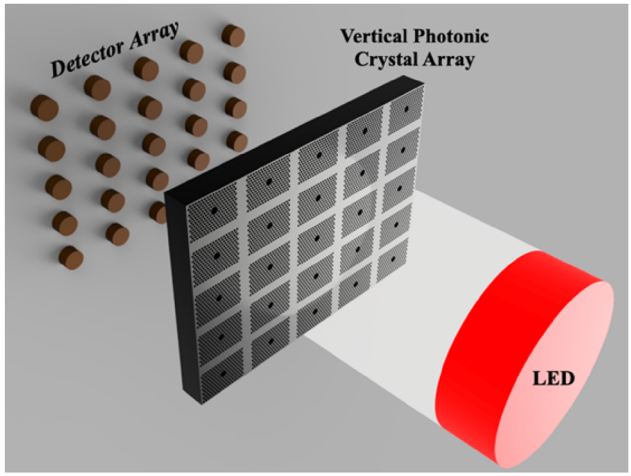

FIG. 11. Schematic illustration of a SUNPCW array configured for multiplexed gas sensing. The sensing process involves (1) gas molecules diffusing into hollow-core defect holes, (2) broadband LED illumination into the waveguides, and (3) measurement of transmitted signals at individual SUNPCW outputs by a detector array.

During sensing operation, broadband mid-infrared radiation from an LED source is vertically coupled into the waveguide array. As the light traverses the gas-filled defect holes, specific wavelengths are selectively absorbed, correlating to the gas molecules' unique absorption spectra. At the output side, a detector array measures the transmitted intensity across individual waveguides, each featuring distinct structural scaling to optimize sensitivity and selectivity toward specific gases. By analyzing and comparing the relative absorption across the different waveguide channels, the sensor accurately identifies and quantifies concentrations of gas species.

This innovative sensing architecture capitalizes on the high group-index properties and enhanced light–matter interactions inherent in silicon-based photonic crystal waveguides. As a result, it demonstrates significant improvements in detection sensitivity and overall performance for mid-infrared gas sensing applications, particularly in compact and portable sensing systems.

IV. CONCLUSION

This work details the development and validation of highly efficient photonic crystal waveguides, with particular focus on air-core modes exhibiting high group indices within vertical photonic crystal waveguide structures. Our approach involved extensive theoretical simulations using two complementary methods: the plane wave expansion method and the finite-difference eigenmode method. These simulations enabled the successful engineering of photonic crystal waveguides consisting of two-dimensional hexagonal lattices of air holes with strategically positioned enlarged air hole defects, designed for efficient operation in the mid-IR region.

The numerical simulations were instrumental in calculating the bandgap map of the vertical photonic crystal structure and optimizing the waveguide design to facilitate slow-light propagation of guided modes based on band structure analysis. Simulation results for photonic crystal waveguide structures operating at absorption wavelengths of 3.31, 4.28, and 4.47 μm demonstrate that group indices can reach values of ~1424, 866, and 698, respectively.

The slow-light effect fundamentally increases the effective optical length, the photon-analyte interaction length, without enlarging the device footprint. This enhancement enables significantly improved absorption sensitivity in compact, chip-scale geometries. The scalable waveguide geometry allows wavelength-selective sensing operation, and when implemented as an array of waveguides (Fig. 11), the platform enables multiplexed detection of multiple gas species on a single chip.

A key advantage of this design is its inherent compactness, eliminating the need for external spectral analysis components in spectroscopic sensing systems and making it particularly suitable for portable mid-IR applications. By combining ultra-high group indices, slow-light-enhanced light-analyte interactions, and wavelength-engineered device geometries, this compact and efficient design represents a significant advancement in integrated photonic gas sensing technology.

ACKNOWLEDGMENTS

We acknowledge support from NASA under Contract No. NASA-80NSSC22PB125.

AUTHOR DECLARATIONS

Conflict of Interest

The authors have no conflicts to disclose.

Author Contributions

Kang-Chieh Fan: Data curation (equal); Methodology (equal); Software (equal); Writing – original draft (equal); Writing – review & editing (equal). **Jason Midkiff**: Conceptualization (equal); Data curation (equal); Investigation (equal); Project administration (equal); Writing – review & editing (equal). **May Hlaing**: Conceptualization (equal); Data curation (equal); Methodology (equal); Writing – review & editing (equal). **Sourabh Jain**: Conceptualization (equal); Formal analysis (equal); Visualization (equal); Writing – review & editing (equal). **Ray T. Chen**: Conceptualization (equal); Funding acquisition (equal); Project administration (equal); Resources (equal); Supervision (equal); Validation (equal); Writing – review & editing (equal).

DATA AVAILABILITY

The data that support the findings of this study are available from the corresponding author upon reasonable request.

REFERENCES

[1]T. A. Birks, J. C. Knight, and P. S. J. Russell, "Endlessly single-mode photonic crystal fiber," Opt. Lett. **22**, 961–963 (1997).
[2]J. C. Knight, T. A. Birks, P. S. J. Russell, and D. M. Atkin, "All-silica single-mode optical fiber with photonic crystal cladding," Opt. Lett. **21**, 1547–1549 (1996).
[3]Y. Jiang, X. Chen, B. Howley, M. Y. Chen, and R. T. Chen, "Effects of temperature fluctuation on highly dispersive photonic crystal fibers," Appl. Phys. Lett. **88**, 011108 (2006).
[4]H. Subbaraman, T. Ling, Y. Jiang, M. Y. Chen, P. Cao, and R. T. Chen, "Design of a broadband highly dispersive pure silica photonic crystal fiber," Appl. Opt. **46**, 3263–3268 (2007).
[5]S. Jain, M. H. Hlaing, K.-C. Fan, J. Midkiff, S. Ning, C. Feng, P.-Y. Hsiao, P.-T. Camp, and R. T. Chen, "Incubating advances in integrated photonics with emerging sensing and computational capabilities," Appl. Phys. Rev. **12**, 011337 (2025).
[6]J. T. Mok and B. J. Eggleton, "Expect more delays," Nature **433**, 811–812 (2005).
[7]C. Liu, Z. Dutton, C. H. Behroozi, and L. V. Hau, "Observation of coherent optical information storage in an atomic medium using halted light pulses," Nature **409**, 490–493 (2001).
[8]M. Y. Chen, H. Subbaraman, and R. T. Chen, "One stage pulse compression at 1554 nm through highly anomalous dispersive photonic crystal fiber," Opt. Express **19**, 21809–21817 (2011).
[9]H. Subbaraman, M. Y. Chen, and R. T. Chen, "Photonic crystal fiber-based true-time-delay beamformer for multiple RF beam transmission and reception of an x-band phased-array antenna," J. Lightwave Technol. **26**, 2803–2809 (2008).
[10]R. F. Cregan, B. J. Mangan, J. C. Knight, T. A. Birks, P. S. J. Russell, P. J. Roberts, and D. C. Allan, "Single-mode photonic band gap guidance of light in air," Science **285**, 1537–1539 (1999).
[11]T. Baba, "Slow light in photonic crystals," Nat. Photonics **2**, 465–473 (2008).
[12]J. Joannopoulos, S. Johnson, J. Winn, and R. Meade, *Photonic Crystals: Molding the Flow of Light*, 2nd ed. (Princeton University Press, Princeton, 2008).
[13]D. Popa and F. Udrea, "Towards integrated mid-infrared gas sensors," Sensors **19**, 2076 (2019).
[14]C. Berthomieu and R. Hienerwadel, "Fourier transform infrared (FTIR) spectroscopy," Photosynth. Res. **101**, 157–170 (2009).

[15]M. Lackner, "Tunable diode laser absorption spectroscopy (TDLAS) in the process industries—A review," Rev. Chem. Eng. **23**, 65–147 (2007).
[16]M. J. Thorpe, K. D. Moll, R. J. Jones, B. Safdi, and J. Ye, "Broadband cavity ringdown spectroscopy for sensitive and rapid molecular detection," Science **311**, 1595–1599 (2006).
[17]P. Patel, M. Hardik, and P. Patel, "A review on photoacoustic spectroscopy," Int. J. Pharm. Erud. **3**, 41–56 (2013).
[18]Z. Zhu and T. Brown, "Full-vectorial finite-difference analysis of microstructured optical fibers," Opt. Express **10**, 853–864 (2002).
[19]E. D. Palik, *Handbook of Optical Constants of Solids* (Academic Press, 1998), Vol. 3.